Journal of The
Electrochemical Society

OPEN ACCESS

Impact of LiF Particle Morphology on Overpotential and Structure of Li Metal Deposition

To cite this article: Rui Guo *et al* 2022 *J. Electrochem. Soc.* **169** 100523

View the article online for updates and enhancements.

You may also like

- Efficient Lithium Metal Cycling at a Wide Range of Pressures from an Anion-Derived Solid-Electrolyte Interphase Framework
Hansen WANG and Yi Cui
- Combinatorial Methods for Improving Lithium Metal Cycling Efficiency
Matthew Genovese, A. J. Louli, Rochelle Weber et al.
- Effects of Carbonate Solvents and Lithium Salts in High-Concentration Electrolytes on Lithium Anode
Yueying Peng, Kei Nishikawa and Kiyoshi Kanamura

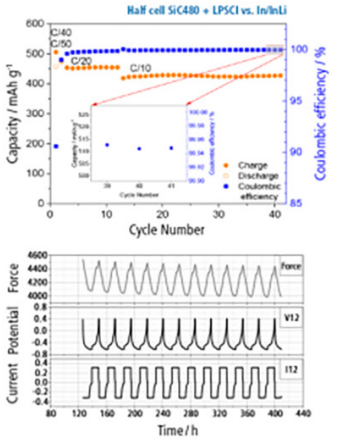
The New PAT-Cell-Solid!

EL-CELL®
electrochemical test equipment

Cycle Solid-State Batteries Under Controlled Pressure of up to 300 MPa (6 mm Diameter)!



- Adjust and measure a force of up to 9000 N on the cell stack!
Force adjustment possible throughout the entire experiment
- Built-in force, and temperature sensors!
With optional gas pressure sensor and gas in- and outlet
- PAT-Solid-Core for easy assembly and reproducible results!
Press and cycle solid-state batteries with 6 or 10 mm electrode diameter
- Cableless and highly sealed battery test cell!
For precise long-term measurements of solid-state cell chemistries



Learn more on our product website:
Scan me!

Download the data sheet (PDF):
Scan me!

Or contact us directly:
+49 40 79012-734
sales@el-cell.com
www.el-cell.com

This content was downloaded from IP address 158.69.193.207 on 12/11/2026 at 11:50

Journal of The Electrochemical Society, 2022 **169** 100523

Impact of LiF Particle Morphology on Overpotential and Structure of Li Metal Deposition

Rui Guo, Kyeong-Ho Kim, and Betar M. Gallant[*,z]

Department of Mechanical Engineering, Massachusetts Institute of Technology, Cambridge, Massachusetts 02139, United States of America

It has been widely suggested in literature that a lithium fluoride (LiF)-rich solid electrolyte interphase (SEI) affects Coulombic efficiency (CE) of the Li metal anode used with liquid electrolytes. Yet, the influence of LiF on Li metal deposition has been challenging to examine. Herein, we developed a method to synthesize LiF nanoscale particles with tunable sizes (30–300 nm) on Cu electrodes by electrochemical reduction of fluorinated gases under controlled discharge rates and capacities. The impact of LiF nanoparticles on overpotential and morphology of Li deposition was further studied in a conventional carbonate electrolyte. By cyclic voltammetry, Li plating overpotentials exhibit a clear correlation with the total surface area of LiF particles. Additionally, Li metal deposits (10 μAh cm^{-2}) nucleated under galvanostatic conditions (0.5 mA cm^{-2}) on Cu/LiF showed increasing feature sizes with a lower average LiF particle size and higher coverage of LiF. However, no significant improvement in CE was observed for LiF-coated Cu. Our findings provide evidence that a particle-based mode of SEI fluorination can influence early-stage Li nucleation to a modest degree, and this effect is maximized when LiF is uniformly and densely distributed. However, sparser and larger LiF have vanishing or even detrimental effect on cycling performance.

© 2022 The Author(s). Published on behalf of The Electrochemical Society by IOP Publishing Limited. This is an open access article distributed under the terms of the Creative Commons Attribution 4.0 License (CC BY, http://creativecommons.org/licenses/by/4.0/), which permits unrestricted reuse of the work in any medium, provided the original work is properly cited. [DOI: 10.1149/1945-7111/ac98e3]

Manuscript submitted August 3, 2022; revised manuscript received September 25, 2022. Published October 18, 2022. *This paper is part of the JES Focus Issue on Nucleation and Growth: Measurements, Processes, and Materials.*

Supplementary material for this article is available online

Li metal is regarded as an ultimate anode material for next-generation Li-ion batteries because of its combination of high gravimetric capacity (3860 mAh g^{-1}) and low potential (−3.04 V vs SHE), enabling batteries that can theoretically exceed 500 Wh kg^{-1}.[1] However, the tendency of textured Li growth, in some cases leading to dendrites,[2,3] results in electrolyte consumption and engenders electronically isolated Li[4] and low Coulombic efficiency (CE) that still falls short of 99.95% required by electric vehicles.[5] The origin of these challenges can be attributed to the poor stability of the solid electrolyte interphase (SEI), a nanoscale layer (tens of nm) that, in carbonate-based electrolytes, is composed of ionic phases (e.g., lithium oxide (Li_2O), lithium fluoride (LiF), lithium carbonate (Li_2CO_3)); semi- and alkyl carbonates (e.g., lithium ethylene dicarbonate ($(CH_2OCO_2Li)_2$); lithium alkyl carbonates ($ROCO_2Li$)); and oligomeric species derived from chemical reactions between Li and electrolyte.[6,7] An ideal Li SEI should be chemically and mechanically stable with fast ionic transport and no electron leakage. Unfortunately, the native Li SEI formed in traditional carbonate electrolytes hardly fulfills these requirements,[8] and researchers have been searching for the most desired components and structures to form a stable Li SEI.

Among key SEI components, lithium fluoride (LiF) has received intense focus.[9] A number of studies have reported that increasing the amount of LiF in the SEI, e.g., by using fluorinated electrolytes or fluorine-donating additives, correlates with increased CE.[10–13] Many experimental findings have further asserted that in situ LiF therefore plays a critical role in improving the Li SEI,[14–18] although LiF functionality remains in dispute.[19] In support of these arguments, researchers have invoked various bulk properties unique to LiF, e.g., its wide electrochemical window (0–6.4 V vs Li/Li$^+$),[20] large band gap (13.6 eV),[21] high surface energy (0.36 J m^{-2} for (001) plane)[22,23] and low Li adatom diffusion barrier (0.19 eV),[24] which have been proposed to suppress Li dendrite growth and/or improve the chemical/mechanical stability of the SEI.[10,12,17,18,25]

It is reasonable to anticipate that bulk LiF properties may, however, overlook or misestimate properties relevant to an SEI in liquid electrolytes, which is microstructured, heterogeneous, and complex. For instance, density functional theory (DFT) calculations by Leung and Jungjohann[26] found that polycrystalline LiF thin films (approximately 10 Å thick) are more resistant to Li filament growth than Li_2O, suggesting its favorability. However, Smeu and Leung,[27] upon further examining electron transport at the grain boundaries (GBs) of polycrystalline LiF, reported 7–9 orders of magnitude higher electronic conductance in the GB region compared to single crystal LiF. Feng et al.[28] also found that GBs between LiF phases have much lower bandgaps compared to the crystalline bulk and can trap electrons, enhancing Li dendrite growth into the SEI. These works collectively indicate that LiF microstructure significantly influences its electronic properties. Additionally, more recent experimental studies of the native SEI using (cryo-) transmission electron microscopy (TEM) have offered new, yet nonconvergent, evidence regarding the relationship between Li CE and the nanostructure of LiF. Jurng et al.[29] reported that an SEI with finer native LiF particles (<10 nm) correlates with more uniform Li$^+$ diffusion field gradients and higher CE than that with larger LiF particles (>300 nm). On the other hand, Huang et al.[30] further revealed that LiF phases generated by fluoroethylene carbonate (FEC) additive, which can improve CE, are in the form of nanoparticles (>100 nm) deposited on the current collector rather than in the compact SEI, and argued that LiF does not govern Li deposition and cycling efficiency. Although cryo-EM has provided powerful initial insights,[30–33] it is still difficult to correlate SEI properties with the LiF phases observed in electron microscopy due to limited statistics.

Herein, we aimed to examine if and how LiF influences Li plating under well-defined and experimentally observable conditions. To do so, a method to decouple the synthesis of LiF nanoparticles from the formation of the native SEI was developed. This approach uniquely affords independent control over the average particle size and distribution of LiF on a Cu current collector with characteristic features reproducible across a centimeter length scale. The LiF nanoparticles were synthesized on Cu substrates via electrochemical reduction of the fluorinated gases nitrogen trifluoride (NF_3) and sulfur hexafluoride (SF_6) under various current densities, and further characterized by X-ray photoelectron spectroscopy (XPS), scanning electron microscopy (SEM) and TEM. The onset potentials for Li metal deposition with or without LiF particles were compared, and variations were interpreted using simplified electrode kinetics analysis. A strong relationship between surface area of LiF nanoparticles and the modulation of Li plating overpotentials is observed. Li deposition morphology was

*Electrochemical Society Member.
[z]E-mail: bgallant@mit.edu

further evaluated under galvanostatic discharge with pre-formed LiF particles on the Cu substrate. Finally, we evaluate this specific LiF system's results against the claim that LiF electronic and ionic properties widely invoked in literature translate to improved performance metrics, namely CE.

Experimental

Chemicals and materials.—All handling of chemicals and materials for cell assembly was conducted in an argon (Ar)-filled glovebox (MBraun) with O_2 and H_2O contamination below 0.1 ppm. Cu foil (9 μm thick, >99.8%, MTI Corporation) was washed with 1 M dilute sulfuric acid (H_2SO_4), copiously rinsed with deionized water, and dried under vacuum at room temperature. Li foil (0.75 mm thick, ⩾99.9% metals basis, Alfa Aesar) was mechanically rolled and punched to discs (11 mm diameter) for cell assembly. Lithium bis(trifluoromethanesulfonyl)imide (LiTFSI, 99.99% trace metals basis, Sigma-Aldrich) and Whatman filter paper (Grade QM-A, 2.2 μm pore size, 450 μm thickness, Sigma-Aldrich) were dried in a glass oven (Buchi) under active vacuum at 120 °C for 24 h. Lithium bis(fluorosulfonyl)imide (LiFSI, >99.9%, Arkema) was dried under active vacuum at 80 °C for 24 h. Dimethyl sulfoxide (DMSO, >99.9%, Sigma-Aldrich), fluoroethylene carbonate (FEC, >99%, TCI), dimethoxymethane (DME, 99.5%, Sigma-Aldrich), 1,3-dioxolane (DOL, 99.8%, Sigma-Aldrich), tetrahydrofuran (THF, ⩾99.9%, Sigma-Aldrich) and 1.0 M $LiPF_6$ EC/DEC = 50/50 (v/v) solution (battery grade, Sigma-Aldrich) were used as received inside the glovebox.

Synthesis of LiF nanoparticles on Cu.—Two-electrode Swagelok-type cells were assembled in an argon glovebox, with cleaned and dried Cu foil (12 mm diameter) as the cathode substrate and Li foil (11 mm diameter) as anode. The cells were modified to contain an inlet and outlet valve and gas headspace to allow for introduction of the reactant gas to cells after battery assembly. A Whatman glass fiber filter paper (13 mm diameter) was used as separator and was impregnated with 60 μl of 0.1 M LiFSI in DMSO. Assembled cells were immediately purged with NF_3 (99.99%, Airgas) or SF_6 (99.999%, Airgas) gas for 1 min, pressurized to 2.0 bar and sealed, which allows for gas to be dissolved in the electrolyte under the headspace pressure. Cells were then discharged galvanostatically (typically 1–10 μA cm^{-2}, based on Cu geometric surface area) at room temperature to a fixed capacity (typically 0.5–2 μAh cm^{-2}). The mass of total LiF particles on the electrodes can be estimated from the discharge capacity ($m_{LiF} = Q_{discharge} \times M_{LiF}/F$, where $Q_{discharge}$ is the discharge capacity in Coulombs, M_{LiF} is molar mass of LiF and F is Faraday constant), assuming that LiF is the major reduction product and dissolution of LiF is negligible. The total surface area of LiF particles (S_{LiF}) is estimated from the average particle diameter (d_{LiF}, diagonals of cubic particles) from SEM images by $S_{LiF} = 10.39 \times m_{LiF}/(d_{LiF} \cdot \rho_{LiF})$, assuming LiF particles are cubic in shape (10.39 results from the geometric relationship between the diagonal and side length of a cube). All electrochemical testing was performed using a Biologic MPG-2 potentiostat. Immediately after the Li-gas cells reached the desired discharge capacity, the cells were evacuated and purged with Ar to remove residual gas and then transferred to the Ar glovebox. The Li-Cu/LiF cells were then dissembled under Ar, and the discharged Cu electrodes were rinsed extensively with THF, dried under vacuum and saved for further analysis or transferred to cells for Li plating experiments.

Li plating via cyclic voltammetry in three-electrode cells.—A Cu foil disc with/without LiF nanoparticles was used as the working electrode in a three-electrode cell (MTI Corporation). Li metal was used as the counter electrode and reference electrode. Three electrode cells were used to avoid any possible interference of the Li working electrode overpotential under CV conditions and allow for the most accurate determination of the plating overpotentials arising at the LiF-modified Cu electrode. Two pieces of Whatman glass fiber filter paper (24 mm diameter) was used as separator in order to be consistent with the Li-gas cells where LiF was prepared on Cu electrodes, and was impregnated with 200 μl commercial carbonate electrolyte, 1 M $LiPF_6$ in EC/DEC. Cyclic voltammetry measurements were conducted with a scan rate of 1 mV s^{-1}. The working electrode potential initiated at open circuit voltage (typically 2.9–3.1 V vs Li/Li$^+$) and was scanned to −0.15 V vs Li/Li$^+$. All measurements were performed on a Biologic MPG-2 potentiostat.

Coulombic efficiency measurements in coin cells.—2032-type coin cells were assembled with a Li anode and Cu cathode with/without LiF nanoparticles. One piece of Whatman glass fiber filter paper (16 mm diameter) was used as separator and was impregnated with 100 μl of 1 M $LiPF_6$ in EC/DEC electrolyte. After assembly the coin cells were galvanostatically cycled at 0.5 mA cm^{-2} to a fixed capacity of 0.5 mAh cm^{-2} or 10 μAh cm^{-2}, and then stripped with a cutoff voltage of 1.0 V. CE was defined as the ratio of stripping capacity to the plating capacity.

Scanning electron microscopy (SEM).—SEM images were taken with a Zeiss Merlin scanning electron microscope at an accelerating voltage of 1–5 kV. Samples with Li metal deposition were transferred to the SEM without exposure to air via a transfer vessel (Semilab Inc.) built for the Zeiss SEM airlock.

Transmission electron microscopy (TEM).—TEM samples were prepared by rubbing the LiF-covered Cu electrodes with a TEM grid supported by lacey carbon. TEM images were taken with a JEOL 2010F analytical transmission electron microscope at an accelerating voltage of 200 kV. The TEM samples were carried by an argon-filled vessel and transferred into the TEM chamber to minimize exposure to air.

X-ray photoelectron spectroscopy (XPS).—XPS analysis was conducted on a PHI VersaProbe II X-ray Photoelectron Spectrometer. Samples were transferred in an air-sensitive transfer vessel to minimize exposure to air. Binding energies were calibrated by the adventitious carbon peak at 284.8 eV.

Results

Electrochemical formation of LiF nanoparticles by fluorinated gases.—The typical coupling between salt and solvent reduction to form a native SEI affords little independent control over LiF morphology and distribution, making the influence of LiF structure on electrochemical behavior challenging to study. In an attempt to overcome this limitation, we exploited the electrochemical reduction of fluorinated gases NF_3 and SF_6 on conductive cathode substrates in Li cells as a means to form well-controlled LiF particles with characteristic and diverse particle sizes and coverage. The methodologies to electrochemically form LiF from these gases on carbon cathodes were previously described in detail elsewhere.[34,35] In brief, the primary cathode discharge reactions for NF_3 and SF_6 reduction have been determined to be as follows: $2NF_3 + 6e^- + 6Li^+ = 6LiF + N_2$ and $SF_6 + 8e^- + 8Li^+ = 6LiF + Li_2S$, respectively, with concurrent oxidation of Li metal at the anode, and typical cell voltages in the range of 2–3 V vs Li. Notably, with NF_3, N_2 is a product gas, and LiF is the only solid-phase discharge product formed, representing an ideal LiF-forming reaction without any solid co-products. In contrast, lithium sulfide and some polysulfides form upon reduction of SF_6 in Li cells. The product sulfur species are relatively minor given the 1/6 ratio of S/F in the reactant, and were found to be highly soluble in DMSO. Previous XPS analysis indicated limited solid sulfur products remained in the cathode even at high depth of discharge.[35] Testing of both NF_3- and SF_6-derived LiF helps to ensure that the behaviors examined are specific to LiF particles and not to their formation pathway.

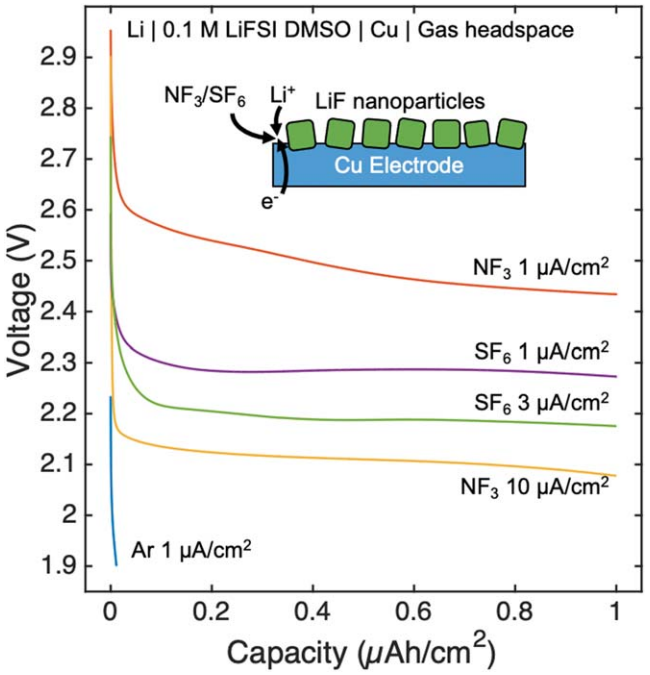


Figure 1. Galvanostatic discharge of Li-NF_3 and Li-SF_6 gas cells with variable current densities (1, 3 or 10 μA cm^{-2}) and the same total capacity of 1 μAh cm^{-2}. The inset shows a schematic of LiF nanoparticles synthesized on a Cu electrode after discharge of the Li-gas cells. A Li-Ar background cell (no fluorinated gas, assembled under Ar only) had negligible capacity, indicating no significant electrolyte decomposition above 1.9 V during the LiF formation process.

Here, we apply these gas reactions on Cu current collectors for the first time. Figure 1 shows NF_3 and SF_6 reduction on Cu at 1 μA cm^{-2} (denoted NF-1 or SF-1), 3 μA cm^{-2} (SF-3) or 10 μA cm^{-2} (NF-10) for a total capacity of 1 μAh cm^{-2} in 0.1 M LiFSI DMSO. Different maximum current densities were used for NF_3 and SF_6 because SF_6 shows more severe losses and less reproducible discharge at higher currents, whereas 10 μA cm^{-2} was chosen for NF_3 (NF-10) to enable greater differentiation in the formed LiF particle sizes; ultimately, the current densities of LiF formation are only critical insofar as they allow generation of varied LiF particle sizes as discussed later. No significant capacity was observed upon discharge under an Ar headspace, i.e. without fluorinated gas, indicating that the activity arose solely from gas reduction. The minimal background capacity also indicates negligible electrolyte decomposition above 1.9 V in the DMSO electrolyte. In both cases, similar discharge voltages were observed on Cu as on carbon cathodes reported previously, i.e. in the 2–3 V range. Additionally, in both cases, higher current density led to a lower discharge plateau, for example 2.1 V vs 2.4 V for NF-10 and NF-1, and 2.2 V vs 2.3 V for SF-3 and SF-1, as expected.

The products formed on the discharged Cu electrodes (Figs. 2a–2b) had discrete particle morphology with variable size depending on the gas precursor and discharge condition. These particles were confirmed to be LiF by XPS (Figs. S1, 2c) and were further confirmed to be polycrystalline with some amorphous phases by TEM selected area diffraction (Fig. S2). Statistical analysis of the SEM images (Fig. 2b) indicated that the LiF particles formed at lower current densities have larger particle sizes and a wider distribution (NF-1 and SF-1: 131 ± 30 and 128 ± 32 nm diagonal, respectively) than those formed at higher current densities (SF-3 and NF-10: 75 ± 13 and 47 ± 16 nm, respectively). Meanwhile, the smaller LiF particles in SF-3 and NF-10 also correspond to more-uniform coverage and less exposed Cu. The XPS analysis indicated larger LiF integrated peak intensity at 685 eV (F 1s) and 56 eV (Li 1s) for electrodes discharged at higher current densities (NF-10 and SF-3) compared to those discharged at lower current densities (NF-1 and SF-1). Beyond LiF, the elemental distributions in Fig. 2c show adventitious carbon and trace amounts of S. The latter was not unique to use of SF_6, hence could be attributed to minor but unavoidable sulfate residuals (Fig. S1) from prior H_2SO_4 cleaning of the Cu surface, which was higher for electrodes with greater fractions of exposed Cu as occurred with larger LiF particle sizes. Consistently, no trace S element was observed in NF-10, the surface exhibiting the highest degree of coverage by LiF. Overall, the characteristic sizes of LiF particles formed using this method are comparable to those observed in native SEI previously, which have been reported to range from tens to hundreds of nanometers depending on the electrolyte and cycling history of the electrode.[29,30,32,36]

Onset potential of Li plating with LiF nanoparticles on Cu.—Li plating on bare or LiF-modified Cu electrodes was next studied in a commercial carbonate electrolyte, 1 M $LiPF_6$ EC/DEC. This electrolyte, notably, avoids fluorinated solvents and excessively fluorine-donating salts such as lithium bis(fluorosulfonyl)imide (LiFSI),[10] which would otherwise be considered to aggressively re-form LiF in the native SEI, although some degree of LiF formation with $LiPF_6$ will undoubtedly occur.[37] Cyclic voltammetry (CV) was conducted at 1 mV s^{-1} from open circuit (Fig. S3) to −0.15 V, resulting in typical Li deposition capacities of ∼15 μAh cm^{-2}. The initial Li plating onset potential (E_p, V vs Li/Li^+) was quantified by linear extrapolation of the CV response to zero plating current (Fig. 3). Notably, E_p varied observably between samples without and with LiF modification. Unexpectedly, E_p was the most negative (approximately −90 mV vs Li/Li^+) for pristine Cu (Fig. 4a), while the presence of LiF particles yielded a consistently higher Li plating potential (lower plating overpotential) that ranged from −76 to −60 mV vs Li/Li^+. This result is surprising as LiF is commonly regarded as an electronic insulator and poor ionic conductor, although reported values vary widely and microstructural features can modify behaviors as discussed in the Introduction.[9,38,39] Regardless, coating of LiF particles (50–130 nm diameter) on Cu was expected to impede, rather than enhance, Li deposition by reducing the active surface area. Additionally, a relationship between the LiF particle size and changes in onset potential compared to pristine Cu (ΔE_p) was observed, where smaller particles and larger total LiF surface area (see Experimental section for calculation details) led to the most significant positive ΔE_p (Fig. 4b). We emphasize that consistent trends were observed regardless of whether SF_6 or NF_3 was used as the precursor gas, hence modulations in plating potential are reflective of intrinsic features of the LiF particles rather than artifacts of their specific synthesis route.

In addition to the samples with controlled LiF discharge capacity but different rate, additional conditions were tested by discharging SF_6 at 1 μA cm^{-2} to variable capacity: 0.5 μAh cm^{-2}, 1 μAh cm^{-2}, and 2 μAh cm^{-2} (Fig. 5a). The size of LiF particles in SF-1(0.5 h) (0.5 μAh cm^{-2}) is similar to that in SF-1(1 h) (1 μAh cm^{-2}), leading to a total LiF surface area in SF-1(1 h) that is approximately doubled, i.e. 0.336 cm^2 at 1 h vs 0.173 cm^2 at 0.5 h (Figs. 5b and 5c). However, the size of LiF particles in SF-1(2 h), corresponding to 2 μAh cm^{-2}, were significantly increased compared to those at lower capacity, with an average diameter over 220 nm. This indicates a transition from increasing numbers of particle nuclei up to 1 μAh cm^{-2} towards continued growth of these nuclei as discharge proceeds, and is further supported by an absence of small particle sizes denoting earlier growth stages at 2 μAh cm^{-2}. Consequently, although the capacity was higher, the larger particle sizes resulted in an only marginally higher total surface area (0.378 cm^2) on this sample compared to SF-1(1 h) (Figs. 5c and 5d). The changes in Li plating onset potentials for the capacity-dependent samples were also measured (Fig. S4) and plotted against the total calculated LiF surface area (Fig. 5e). The data points align well with across both experiment sets (Figs. 4–5), showing a strong positive relationship between LiF surface area and the overpotential for Li deposition.

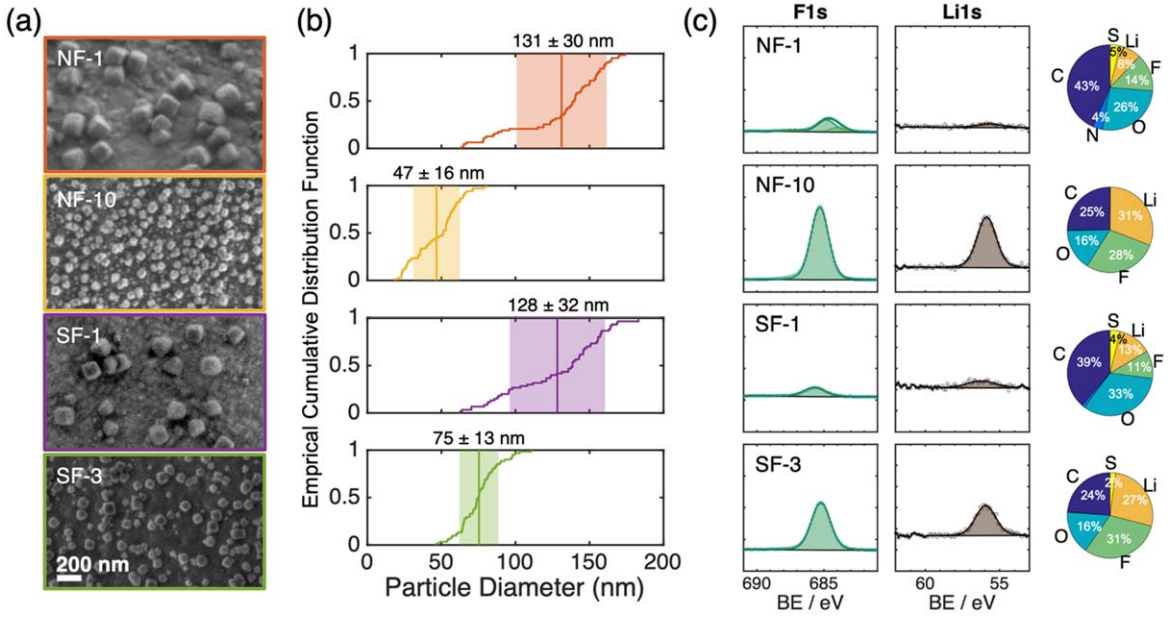


Figure 2. (a) SEM images of LiF nanoparticles formed on Cu electrodes after discharge in Li-NF_3 or Li-SF_6 cells. The bare spaces between particles are uncoated Cu. (b) Empirical cumulative distribution functions of the LiF nanoparticle diameters (the largest diagonals of cubic particles) measured from over 60 particles in each sample. The vertical lines and shaded area in (b) indicate the mean values and standard deviations. Samples correspond horizontally to those in (a). (c) F 1s and Li 1s high-resolution scans with the same range of arbitrary intensity on *y*-axis, and atomic ratios (C, N, O, F, Li, S) obtained from XPS survey scans of each sample.

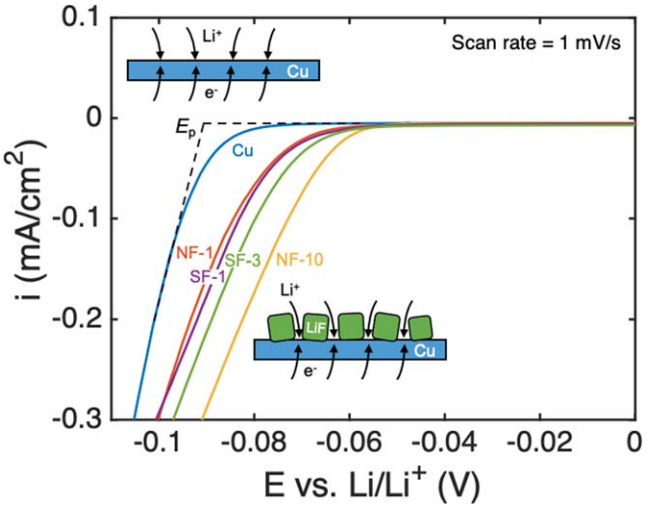


Figure 3. Initial Li plating cathodic scan of Cu electrodes without (blue) or with (red, purple, green, or yellow) LiF particles synthesized by fluorinated gases. Measurements were conducted in a 3-electrode cell with a Li metal counter and reference electrode and 1 M $LiPF_6$ in EC/DEC electrolyte. The onset potentials for Li plating (E_p) were obtained by linear extrapolation of the reduction current to zero current.

Relationship between LiF surface area and Li plating overpotential.—Experimental observations in the previous section indicate a positive, monotonic relationship (Fig. 5e) between the surface area of LiF particles and the changes in the onset potential for Li plating (ΔE_p). Here, to better understand the origin of this potential change, quantitative parameters are extracted from the CV data by dividing the overpotential into discrete contributions.[40,41] At the electrode level, the total overpotential η (defined with respect to 0 V vs Li/Li^+; negative for Li plating) is attributed to three terms as shown in Eq. 1: charge transfer overpotential η_{ct}, heterogeneous nucleation overpotential η_n, and ohmic loss η_{ohm}. This approach implicitly combines contributions from SEI and electrolyte ohmic resistances into a single term, η_{ohm}, instead of treating them separately as has been done elsewhere,[40] given lack of information on microscopic interfacial parameters needed to analytically model their discrete contributions. Mass transport losses are also neglected in this low-overpotential, low-current region.[42] The nucleation overpotential η_n in Eq. 1 considers the thermodynamic barrier to initiate nucleation.

$$\eta = \eta_{ohm} + \eta_{ct} + \eta_n \quad [1]$$

The charge transfer overpotential η_{ct} is related to the current density i (negative for Li plating) in the Butler-Volmer equation as shown in Eq. 2,

$$i = -i_0\left[e^{-\frac{\alpha F\eta_{ct}}{RT}} - e^{\frac{(1-\alpha)F\eta_{ct}}{RT}}\right] \quad [2]$$

where R is the universal gas constant, T is temperature, α is the cathodic charge transfer coefficient, i_0 is the exchange current density and F is the Faraday constant. An approximation of the explicit form of the charge transfer overpotential is given in Eq. 3,[43]

$$\eta_{ct} \approx \frac{2RT}{F}\sinh^{-1}\left[\frac{i}{2i_0}\exp\left(\frac{\alpha - 0.5}{\alpha}\sinh^{-1}\left(\frac{i}{2i_0}\right)\right)\right] \quad [3]$$

which has been proposed to be more accurate for asymmetric values of the charge transfer coefficient α, i.e. those deviating from the common assumption that $\alpha = 0.5$. Indeed, we estimated α as consistently being in the range of ~0.6 from Tafel slopes (Figs. S5 and S6), which agrees with values reported elsewhere for Li plating in carbonate electrolytes.[44]

The resulting total expression is summarized in Eq. 4:

$$\eta = \frac{2RT}{F}\sinh^{-1}\left[\frac{i}{2i_0}\exp\left(\frac{\alpha - 0.5}{\alpha}\sinh^{-1}\left(\frac{i}{2i_0}\right)\right)\right] + iR_{ohm} + \eta_n \quad [4]$$

which can be fit to the current-potential relations observed in CV scans (Fig. 3), providing values for fitting parameters i_0, R_{ohm} and η_n

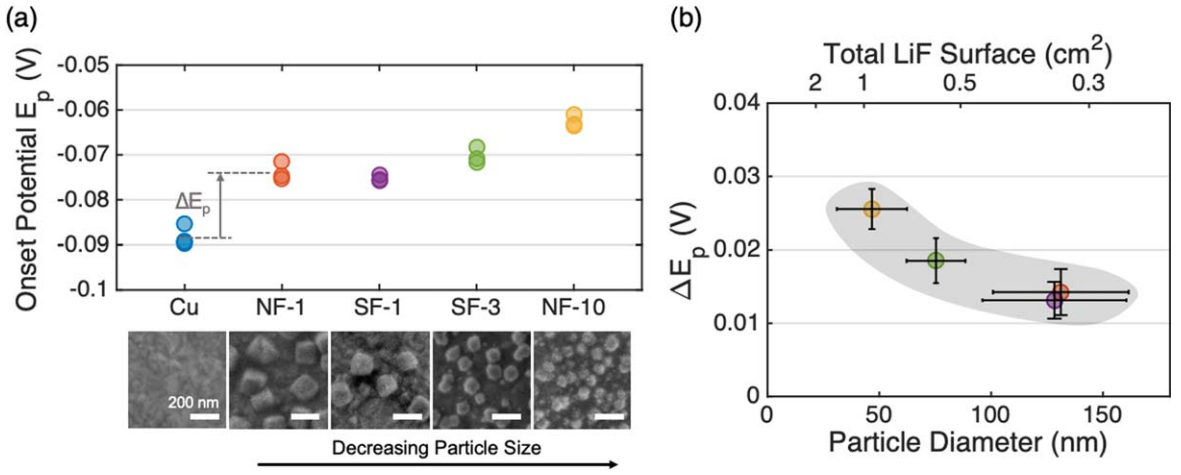


Figure 4. (a) Onset potential of Li plating determined from the initial cathodic scan of Cu electrodes without (blue) or with (red, purple, green, or yellow) LiF. Summary SEM images of LiF particles are included under the sample labels. ΔE_p is the difference of the Li plating potential for a given sample compared to that of uncoated Cu. (b) Relationship between ΔE_p and the average diameter of LiF particles. The horizontal and vertical error bars are from the standard deviation of particle sizes measured by SEM images (>60 particles for each sample) or differences in onset potential measured by CV experiments (3 cells for each sample), respectively.

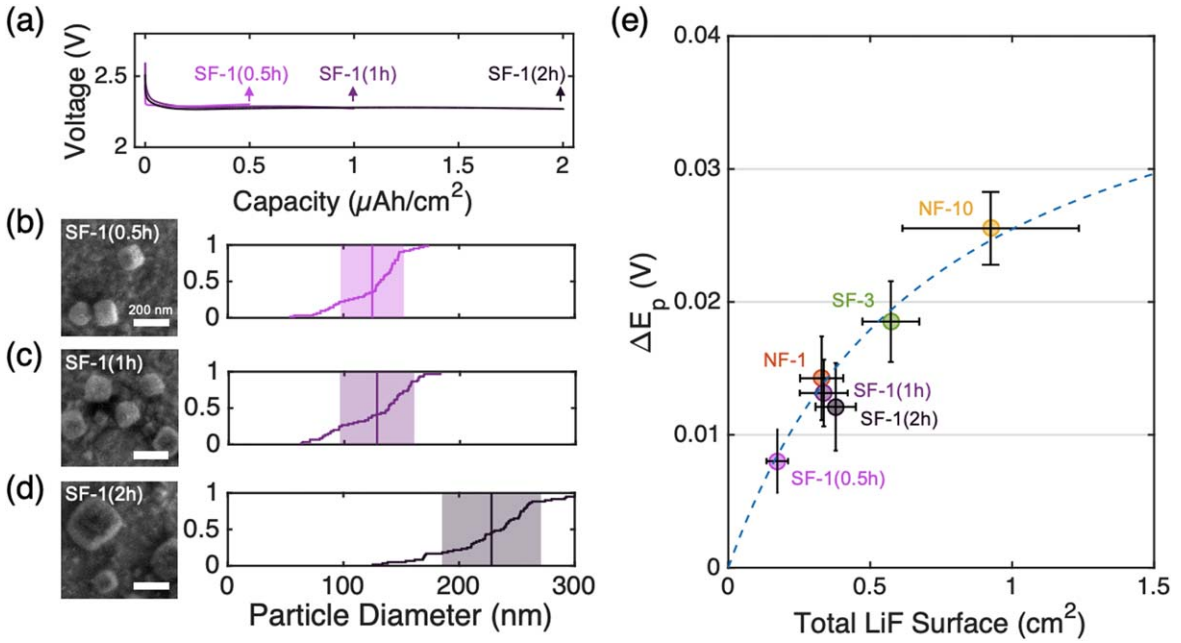


Figure 5. (a) Voltage profiles of Li-SF_6 gas cells with the same current density (1 μA cm^{-2}) but various times (0.5 h, 1 h or 2 h), leading to different total capacities (0.5, 1 and 2 μAh cm^{-2}). (b)–(d) SEM images and empirical cumulative distribution functions of LiF particles as formed during discharge in (a). (e) The relationship between total LiF surface area and the changes in Li plating onset potential compared to that of pristine Cu (ΔE_p). The horizontal and vertical error bars are from the standard deviation of LiF particle surface area estimated from SEM images (>60 particles for each sample) or differences in onset potential measured by CV experiments (3 cells for each sample), respectively. The blue dashed line is a guide to the eye.

(all overpotentials are defined with respect to 0 V vs Li/Li$^+$). High accuracy of this model fit (dashed lines) is obtained in the current density–potential relationship as shown in Fig. 6a. The individual contributions of nucleation, charge transfer and ohmic overpotentials are explicitly graphed for the pristine Cu sample (Fig. 6a) in the fitting region (-0.88 mA cm$^{-2} < i < -0.13$ mA cm^{-2}) and can be similarly deconvoluted for the LiF particle samples.

The fitting outcomes are shown in Figs. 6b–6d and plotted against the total surface area of LiF on the Cu electrode. The results showed no significant change in i_0 (Fig. 6b) when LiF particles were present on the Cu electrode. The comparable i_0 values without and with LiF are counter to expectations if LiF is a purely blocking phase, which should lead to lower total active area available for coupled electron/ion exchange. Hence, while the origins of this observation remain unclear at a microscopic level, we tentatively suggest that LiF is either active, to a degree, for charge transfer, or that its introduction somehow does not physically impede i_0 of the underlying Cu. We note that the relatively constant value of i_0 across samples could be reproduced using a second, independent impedance technique (see Fig. S7 and associated discussion), although the magnitudes were slightly different. Meanwhile, the ohmic resistance (R_{ohm}, Fig. 6c) and nucleation overpotential (η_n, Fig. 6d) were found to exhibit stronger correlations with the total surface area of LiF. Specifically, R_{ohm} increased from 15 Ω for pristine Cu, to 40 and 58 Ω with LiF particles in NF-1 and NF-10, respectively. The increase in ohmic resistance largely accounts for the changes in *i-V* slope observed in Fig. 6a, consistent with our previous findings and others' that nanostructured LiF exhibits low

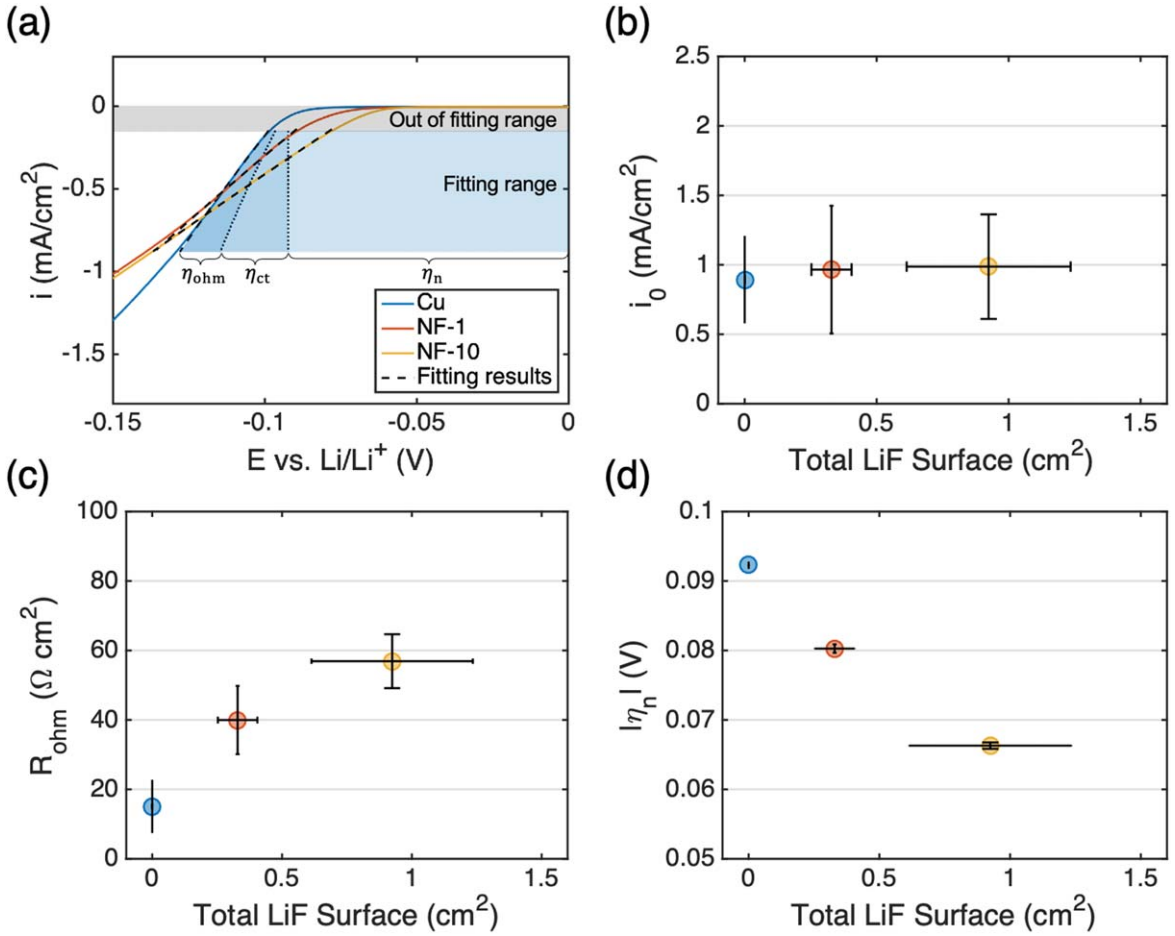


Figure 6. (a) Fitting results of the initial cathodic scan of Cu electrodes with or without LiF nanoparticles (pristine Cu, NF-1 and NF-10) based on the model described in Eq. 4. At low current density ($|i| < 0.1$ mA cm^{-2}), the current-potential relationship was out of fitting range (shaded in gray), possibly due to transition from background capacitive current to Li deposition during the initial cathodic scan. (b) Exchange current density, (c) ohmic resistance and (d) absolute value of nucleation overpotential acquired from the fitting results vs the total surface area of LiF nanoparticles. The vertical error bars are the 95% confidence bounds of the fitting results.

ionic conductivity in the SEI.[39,45] Despite the observed positive trend with LiF surface area, R_{ohm} has, however, little impact on ΔE_p (Fig. 5e) which is measured at near-zero current. On the other hand, the absolute value of nucleation overpotential (Fig. 6d) obtained from our fitting decreased from 92 mV to 67 mV as the total LiF surface area increased from 0 (pristine Cu) to 0.9 cm^2 (NF-10). This is similar, although not identical to, E_p values obtained from visual extrapolation from Fig. 4a (absolute values of 88 and 62 mV, Fig. 4), in which contributions to overpotential remain convoluted. Hence, this straightforward model not only provides quantitative values for key parameters affecting overpotentials, but more importantly, confirms that the observed ΔE_p changes mainly originates from modification of nucleation behavior.

Li deposition morphology and CE with LiF nanoparticles.— Early-stage Li metal deposition morphology was next investigated under galvanostatic discharge at moderate current density (0.5 mA cm^{-2}) and constant low capacity (10 μAh cm^{-2}). This capacity is roughly comparable to that occurring on a typical CV plating step (~15 μAh/cm^2), and approximately ten times that of the LiF capacity (estimated at ~1.0 μAh cm^{-2} and ~0.75 μAh cm^{-2}, assuming 6/6 e$^-$ yield and 6/8 e$^-$ yield of LiF for NF_3 and SF_6, respectively)[34,35] used in Fig. 7, thus is high enough to provide significant information on Li formation statistics but low enough to plausibly see effects from the underlying LiF. Consistently with prior results, the overpotential for galvanostatic Li deposition significantly decreased with LiF particles present, e.g., from 350 mV vs Li on pristine Cu to 130 mV vs Li on NF-10 (Fig. S8). SEM images (Figs. 7a–7d and S9) on bare Cu indicated hexagonal to round-shaped Li nuclei morphologies (200–300 nm in diameter), with relatively sparse Li whiskers grown on top of some Li particles (Fig. 7a). With LiF particles in NF-1 (Figs. 7b–7d), Li deposits at the same capacity were similar in morphology and diameter, but were more irregular-shaped and sparser compared to pristine Cu. With yet-smaller LiF on SF-3 and NF-10, larger Li deposits with diameters over 500 nm were found for fixed capacity, and whisker-like or mossy Li growth appeared more abundant on top of the larger Li deposits. Across all LiF coated samples, no Li deposition was found to occur beneath LiF particles, i.e. no obvious LiF particles were observed on top of the Li deposits. Additionally, numerous bare LiF particles were observed remaining on the Cu substrate (see coloring in Figs. 7b–7d; LiF particles were identified by their cubic shape, which were distinct from the underlying microtexture of Cu foils which is also evident in the images). These observations suggest that LiF is not functioning consistently as a site for preferential Li formation.

Finally, CE of Li plating/stripping was compared for a representative NF-10 sample and bare Cu. At low cycling capacity of 10 μAh cm^{-2} (Fig. 7e), LiF-modified surfaces exhibited initially comparable CE to bare Cu, but CE degraded more readily than bare Cu after the 13th cycle. At a higher cycling capacity (0.5 mAh cm^{-2}, Fig. 7f), no differences were observed between the LiF-covered and bare Cu samples over all 30 cycles tested. Hence, the LiF impacts become less significant when the $Li_{deposited}$/LiF ratio becomes increasingly large. Overall, earlier-stage Li deposits appear to

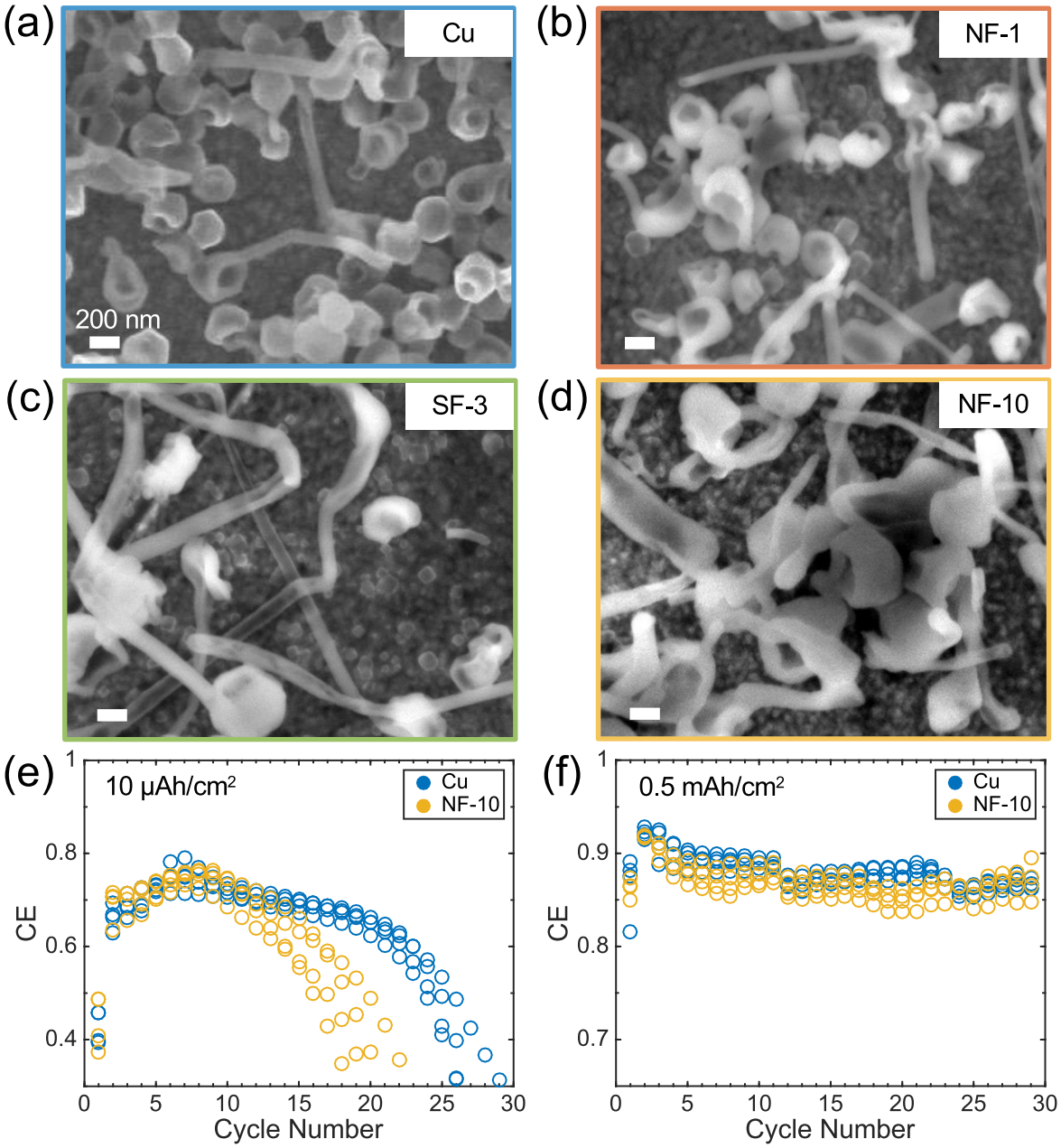


Figure 7. (a)–(d) SEM images of Li metal galvanostatically deposited on (a) bare Cu or on LiF-coated Cu: (b) NF-1, (c) SF-3 and (d) NF-10. liF particles are artificially colored in green for better visualization. See Fig. S10 for original images. Li metal deposition was performed in 1 M $LiPF_6$ EC/DEC at 0.5 mA cm^{-2} with a total capacity of 10 μAh cm^{-2}. (e)–(f) CE measured in Li/Cu coin cells without or with LiF particles in 1 M $LiPF_6$ EC/DEC at 0.5 mA cm^{-2} and capacities of: (e) 10 μAh cm^{-2} or (f) 0.5 mAh cm^{-2}.

experience more influence from the surrounding surface composition and structure on the SEI/Cu current collector than later-stage deposits, given that higher-capacity plating involves structures that grow away from the interface and transition to Li growth on existing Li nuclei.

Discussion

Whether LiF surfaces provide good wettability with Li metal under realistic Li cycling conditions is still in dispute. DFT calculations by Liu et al.[23] and Fan et al.[25] suggested that LiF has a higher interfacial energy in contact with Li metal compared to a similar Li|Li_2CO_3 interface, and therefore Li|LiF interfaces are disfavored where other interfaces can be formed. On the other hand, Tang et al.[46] combined DFT and experimental findings and suggested that LiF coating on LLZO wets molten Li very well with a small contact angle (38°), while Sharafi et al.[47] showed that Li_2CO_3 is much more difficult to wet by molten Li with a large contact angle of 142°. Although it is still not clear whether LiF can provide better wettability for Li deposition compared to other phases in the native SEI, our results indicated that the pristine Cu substrate has higher nucleation barriers for Li metal than LiF particles formed herein. Indeed, Wang et al.[48] reported poor wettability of molten Li on pristine Cu with a large contact angle of 140°, although surface composition of Cu may vary depending on treatment methodologies and between laboratories.[49] Our experimental results imply that surfaces of ex situ LiF can wet Li metal better than pristine Cu and lead to lower nucleation overpotentials. Yet, the SEM images of Li deposition herein (Figs. 7b–7d) did not show direct evidence of preferential Li nucleation on LiF particles, necessitating consideration of other possible explanations. Recalling that the LiF particles formed herein will ultimately become embedded in a native SEI upon polarization of the Cu current collector to reducing potentials,

we suspect that invoking prior models of two-phase interactions defining the relevant surface energies is too reductive for a real SEI that contains multiple and competitive interactions between Li/LiF, Li/Cu, Li/native SEI, LiF/native SEI, and so on.

Jurng et al.[29] proposed that LiF particles with nanoscale sizes (5–10 nm) distributed throughout an SEI can modify the Li^+ diffusion field at the electrode surface, which may arise by redirecting and concentrating Li^+ flux through constrained regions normal to the Cu surface. Such a concentration effect can plausibly lead to higher local supersaturation of Li^+ in the vicinity of LiF particles, lowering the energy barrier for Li nucleation. Our findings indicate that once Li nuclei successfully form on the electrode, Li metal preferentially deposits on those Li nuclei instead of continuously on LiF particles. This is supported by the exacerbated transition from spherical nuclei to whisker morphology occurring on Cu/LiF surfaces, denoting later stages of Li-on-Li deposition triggered by influence of the native SEI.[50]

While this study has examined one specific morphology of LiF particles, it is important to recall that the native SEI consists of phase morphologies that may range from discrete polycrystalline agglomerates[29,30,36] or layers[15,19,51] to nanocrystalline or amorphous phases embedded in a complex matrix.[52,53] Hence, our results are most relevant for systems that form discrete LiF particles and cannot rule on systems that result in more amorphous or uniformly distributed fluorinated interphases. Additionally, the electrolyte used herein (1 M $LiPF_6$ EC/DEC) is not highly fluorinated, thus the insights gained here relate most clearly to conditions in which LiF particles are preexisting on the Cu surface, such as after long cycling, rather than scenarios in which LiF formation occurs continuously in a native SEI. With these caveats, it may be postulated that nanoscale LiF particles in entirely native SEI could similarly reduce Li nucleation overpotential and influence early-stage Li deposition, if they remain in contact with the current collector, although further experimental efforts are needed. Overall, while our results have lent some credence to the fact that LiF can alter the electrochemical and transport properties at the electrode/electrolyte interface, e.g., by lowering nucleation energy barriers and increasing ohmic resistances, LiF particles do not obviously provide any benefit to Li cycling reversibility under the conditions studied herein. On the other hand, they seem relatively well-tolerated when the LiF capacity is low compared to the capacity of cycled Li.

Conclusions

LiF particles with variable characteristic sizes ranging from 30 to 300 nm were synthesized on Cu current collectors through electrochemical reduction of fluorinated gases. The onset potentials for Li plating during CV scans increased significantly, by up to 26 mV, with LiF particles present. The trend in plating potential exhibits a strong positive relationship with the total surface area of LiF. This trend was also found to result in larger initial Li deposition with increasing LiF surface area and decreasing nucleation overpotential. While LiF can modulate Li deposition overpotentials, a negligible impact on CE at capacities prior to failing was observed, i.e., 0.5 mAh cm^{-2} (first 30 cycles) and 10 μAh cm^{-2} (first 13 cycles). Our findings suggested that while LiF can modulate near-field behaviors, which can potentially include Li^+ diffusional field lines and early nucleation processes in the vicinity of LiF, the impact of LiF particles diminishes as Li deposition capacity becomes large and as the active electrochemical interfaces transition to become dominated by deposited Li/native SEI/electrolyte interactions at the expense of Li/LiF (or Li/Cu) interactions. Hence, while our results lend some credence to literature arguments about the impact of LiF on Li deposition electrochemistry, we conclude that remnant, discrete LiF particles in the SEI, as captured by the morphologies herein, do not appear to be a beneficial SEI motif for improving performance.

Acknowledgments

R. G. is supported by MIT Energy Initiative Graduate Student Fellowship. This work made use of the MRSEC Shared Experimental Facilities at MIT, supported by the National Science Foundation under award number DMR-1419807.

ORCID

Rui Guo https://orcid.org/0000-0002-8826-2456
Betar M. Gallant https://orcid.org/0000-0002-4586-2769

References

1. J. Liu et al., *Nat. Energy*, **4**, 180 (2019).
2. K. L. Jungjohann, R. N. Gannon, S. Goriparti, S. J. Randolph, L. C. Merrill, D. C. Johnson, K. R. Zavadil, S. J. Harris, and K. L. Harrison, *ACS Energy Lett.*, **6**, 2138 (2021).
3. F. Hao, A. Verma, and P. P. Mukherjee, *J. Mater. Chem. A*, **6**, 19664 (2018).
4. C. Fang et al., *Nature*, **572**, 511 (2019).
5. G. M. Hobold, J. Lopez, R. Guo, N. Minafra, A. Banerjee, Y. S. Meng, Y. Shao-Horn, and B. M. Gallant, *Nat. Energy*, **6**, 951 (2021).
6. E. Peled and S. Menkin, *J. Electrochem. Soc.*, **164**, A1703 (2017).
7. L. N. Wang et al., *Nat. Chem.*, **11**, 789 (2019).
8. H. P. Wu, H. Jia, C. M. Wang, J. G. Zhang, and W. Xu, *Adv. Energy Mater.*, **11**, 2003092 (2021).
9. J. Tan, J. Matz, P. Dong, J. F. Shen, and M. X. Ye, *Adv. Energy Mater.*, **11**, 2100046 (2021).
10. L. M. Suo, W. J. Xue, M. Gobet, S. G. Greenbaum, C. Wang, Y. M. Chen, W. L. Yang, Y. X. Li, and J. Li, *Proc. Natl Acad. Sci. USA*, **115**, 1156 (2018).
11. X. L. Fan et al., *Nat. Nanotechnol.*, **13**, 715 (2018).
12. W. J. Xue et al., *Energy Environ. Sci.*, **13**, 212 (2020).
13. Z. Yu et al., *Nat. Energy*, **7**, 94 (2022).
14. D. C. Lin, Y. Y. Liu, W. Chen, G. M. Zhou, K. Liu, B. Dunn, and Y. Cui, *Nano Lett.*, **17**, 3731 (2017).
15. J. Zhao et al., *J. Am. Chem. Soc.*, **139**, 11550 (2017).
16. C. Y. Fu and C. Battaglia, *ACS Appl. Mater. Interfaces*, **12**, 41620 (2020).
17. S. Choudhury and L. A. Archer, *Adv. Electron. Mater.*, **2**, 1500246 (2016).
18. Y. Y. Lu, Z. Y. Tu, and L. A. Archer, *Nat. Mater.*, **13**, 961 (2014).
19. M. He, R. Guo, G. M. Hobold, H. Gao, and B. M. Gallant, *Proc. Natl Acad. Sci. USA*, **117**, 73 (2020).
20. W. D. Richards, L. J. Miara, Y. Wang, J. C. Kim, and G. Ceder, *Chem. Mater.*, **28**, 266 (2016).
21. D. M. Roessler and W. C. Walker, *J. Phys. Chem. Solids*, **28**, 1507 (1967).
22. J. J. Gilman, *J. Appl. Phys.*, **31**, 2208 (1960).
23. Z. Liu, Y. Qi, Y. X. Lin, L. Chen, P. Lu, and L. Q. Chen, *J. Electrochem. Soc.*, **163**, A592 (2016).
24. J. H. Zheng, Z. J. Ju, B. L. Zhang, J. W. Nai, T. F. Liu, Y. J. Liu, Q. F. Xie, W. K. Zhang, Y. Wang, and X. Y. Tao, *J. Mater. Chem. A*, **9**, 10251 (2021).
25. X. L. Fan, X. Ji, F. D. Han, J. Yue, J. Chen, L. Chen, T. Deng, J. J. Jiang, and C. S. Wang, *Sci. Adv.*, **4**, eaau9245 (2018).
26. K. Leung and K. L. Jungjohann, *J. Phys. Chem. C*, **121**, 20188 (2017).
27. M. Smeu and K. Leung, *Phys. Chem. Chem. Phys.*, **23**, 3214 (2021).
28. M. Feng, J. Pan, and Y. Qi, *J. Phys. Chem. C*, **125**, 15821 (2021).
29. S. Jurng, Z. L. Brown, J. Kim, and B. L. Lucht, *Energy Environ. Sci.*, **11**, 2600 (2018).
30. W. Huang, H. Wang, D. T. Boyle, Y. Z. Li, and Y. Cui, *ACS Energy Lett.*, **5**, 1128 (2020).
31. Y. Z. Li et al., *Science*, **358**, 506 (2017).
32. X. F. Wang et al., *Nano Lett.*, **17**, 7606 (2017).
33. Y. Z. Li, W. Huang, Y. B. Li, A. Pei, D. T. Boyle, and Y. Cui, *Joule*, **2**, 2167 (2018).
34. M. He, Y. Li, R. Guo, and B. M. Gallant, *J. Phys. Chem. Lett.*, **9**, 4700 (2018).
35. H. Gao, Y. Li, R. Guo, and B. M. Gallant, *Adv. Energy Mater.*, **9**, 1900393 (2019).
36. Z. L. Brown, S. Jurng, C. C. Nguyen, and B. L. Lucht, *ACS Appl. Energy Mater.*, **1**, 3057 (2018).
37. S. K. Heiskanen, J. Kim, and B. L. Lucht, *Joule*, **3**, 2322 (2019).
38. J. Pan, Y. T. Cheng, and Y. Qi, *Phys. Rev. B*, **91**, 134116 (2015).
39. R. Guo and B. M. Gallant, *Chem. Mater.*, **32**, 5525 (2020).
40. P. Biswal, S. Stalin, A. Kludze, S. Choudhury, and L. A. Archer, *Nano Lett.*, **19**, 8191 (2019).
41. A. Pei, G. Y. Zheng, F. F. Shi, Y. Z. Li, and Y. Cui, *Nano Lett.*, **17**, 1132 (2017).
42. F. F. Shi, A. Pei, A. Vailionis, J. Xie, B. F. Liu, J. Zhao, Y. J. Gong, and Y. Cui, *Proc. Natl Acad. Sci. USA*, **114**, 12138 (2017).
43. P. Vijay and M. O. Tade, *Comput. Chem. Eng.*, **102**, 2 (2017).
44. Y. S. Li and Y. Qi, *Energy Environ. Sci.*, **12**, 1286 (2019).
45. C. L. Li, L. Gu, and J. Maier, *Adv. Funct. Mater.*, **22**, 1145 (2012).
46. S. J. Tang, G. W. Chen, F. C. Ren, H. C. Wang, W. Yang, C. X. Zheng, Z. L. Gong, and Y. Yang, *J. Mater. Chem. A*, **9**, 3576 (2021).
47. A. Sharafi, E. Kazyak, A. L. Davis, S. H. Yu, T. Thompson, D. J. Siegel, N. P. Dasgupta, and J. Sakamoto, *Chem. Mater.*, **29**, 7961 (2017).
48. S. H. Wang et al., *Nat. Commun.*, **10**, 4930 (2019).
49. S. Menkin, C. A. O'Keefe, A. B. Gunnarsdottir, S. Dey, F. M. Pesci, Z. H. Shen, A. Aguadero, and C. P. Grey, *J. Phys. Chem. C*, **125**, 16719 (2021).
50. A. Kushima, K. P. So, C. Su, P. Bai, N. Kuriyama, T. Maebashi, Y. Fujiwara, M. Z. Bazant, and J. Li, *Nano Energy*, **32**, 271 (2017).
51. L. Chen et al., *ACS Appl. Mater. Interfaces*, **10**, 26972 (2018).
52. X. Cao et al., *Nat. Energy*, **4**, 796 (2019).
53. Z. Shadike et al., *Nat. Nanotechnol.*, **16**, 549 (2021).